Diffusion of Halogens (F, Cl, Br, I) in silicic melt

Yves Feisel[a]*, Jonathan M. Castro[a], Christoph Helo[a], Anne-Sophie Bouvier[b], Thomas Ludwig[c], Donald B. Dingwell[d,e]

[a] Institut für Geowissenschaften, Johannes Gutenberg-Universität Mainz, 55128 Mainz, Germany

[b] Institut de Sciences de la Terre, University of Lausanne, 1015 Lausanne, Switzerland

[c] Institut für Geowissenschaften, Universität Heidelberg, 69120 Heidelberg, Germany

[d] Department für Geo- und Umweltwissenschaften, Ludwig-Maximilians-Universität München, 80333 München, Germany

[e] Gutenberg Research College, Johannes Gutenberg-Universität Mainz, 55128 Mainz, Germany

***Corresponding authors: yfeise02@uni-mainz.de ; castroj@uni-mainz.de**

Diffusion of halogens (F, Cl, Br, I) in silicic melt

Yves Feisel[a], Jonathan M. Castro[a], Christoph Helo[a], Anne-Sophie Bouvier[b], Thomas Ludwig[c], & Donald B. Dingwell[d,e]

[a] Institut für Geowissenschaften, Johannes Gutenberg-Universität Mainz, 55128 Mainz, Germany

[b] Institut de Sciences de la Terre, University of Lausanne, 1015 Lausanne, Switzerland

[c] Institut für Geowissenschaften, Universität Heidelberg, 69120 Heidelberg, Germany

[d] Department für Geo- und Umweltwissenschaften, Ludwig-Maximilians-Universität München, 80333 München, Germany

[e] Gutenberg Research College, Johannes Gutenberg-Universität Mainz, 55128 Mainz, Germany

Abstract

Chemical diffusion of the halogens F, Cl, Br, and I in silica-rich natural melts was experimentally investigated by the diffusion couple technique. Experiments were conducted under anhydrous conditions at atmospheric pressure and hydrous conditions (~1.5 wt.% H_2O) at 160 MPa, over a temperature range of 750–1000 °C and 1000–1200 °C, respectively. Quenched trachytic melt samples were analyzed using an electron microprobe (EPMA) and secondary ion mass spectrometry (SIMS).

All halogens exhibit Arrhenian behavior during diffusion in the investigated melt compositions with F always diffusing fastest. The other halogens show progressively slower diffusion (F > Cl > Br > I) correlated to their ionic radii. In anhydrous melt a diffusivity range of 3–4 orders of magnitude is covered among the halogens with D_F(1000 °C) ~5×10^{-13} m^2s^{-1} and D_I(1000 °C) ~1×10^{-16} m^2s^{-1}. The diffusivities of all halogens increase in hydrous melt yielding for example D_F(1000 °C) ~ 3×10^{-12} m^2s^{-1}. However, the largest increase is observed for the slowest-diffusing halogens, resulting in a narrower overall diffusive range of only 1–2 orders of magnitude with iodine diffusivity yielding D_I(1000 °C) ~9×10^{-15} m^2s^{-1}. Activation energies (E_A) of all halogens consistently range from ~200–290 kJ mol^{-1} in anhydrous melts.

In hydrous melt E_A generally decreases, with the highest decrease determined for F (~131 kJ mol^{-1}) and only slight changes for the other halogens (~201–222 kJ mol^{-1}).

Our diffusivity data of the anhydrous series exhibit a pronounced correlation of diffusivity with the ionic radii, suggesting that halogen diffusion in highly polymerized melt is closely related to the melt's ionic porosity. The correlation between diffusivity and ionic radius is only weakly observed in the hydrous experiments indicating that the ionic porosity is sufficiently large to weaken the rate-limiting effect of the ionic radius due to the more depolymerized melt structure in the hydrous case. In hydrous experiments, the process of ionic detachment becomes more important as a rate-limiting diffusion mechanism, comparable to the case of diffusion of divalent/trivalent cations or halogen diffusion in basaltic melt.

The results of this study provide the first consistent diffusion dataset including all halogens under naturally relevant magmatic conditions and highlight the pronounced compositional effect of both, major element and dissolved H_2O on halogen diffusion. These data emphasize the potential of diffusive fractionation among the halogens, especially in a melt of low water content, which may be applied as a monitoring tool for volcanic unrest on actively degassing volcanoes.

Keywords: *halogens (F, Cl, Br, I); diffusion couple; ionic porosity; iodine; silicate melt*

1. Introduction

Volatiles are among the most influential constituents of natural silicate magmas. They affect various chemical and rheological melt parameters, which in turn have crucial implications for individual volcanic eruption behavior. Typically, volcanic volatiles are dominated by water (H_2O) and carbon dioxide (CO_2), however, sulfur-species (e.g., SO_2) and halogens, mainly F and Cl, can reach significant concentrations (up to few wt.%) in

78 silicic melts and volcanic gases (e.g., Aiuppa et al., 2009; Dolejš and Zajacz, 2018).
79 Halogens are known to exert strong effects on the physico-chemical properties of silicate
80 melts such as melt viscosity or phase equilibria (e.g., Manning, 1981; Mysen and Virgo,
81 1985; Webster et al., 2018). For example, F is known to reduce the viscosity of silicic melts
82 to a similar degree as added H_2O (Dingwell et al., 1985; Dingwell and Hess, 1998; Zimova
83 and Webb, 2007; Giordano et al., 2008; Baasner et al., 2013), and can depress the isobaric
84 liquidus temperature in basalt (e.g., Filiberto et al., 2012) and felsic melts (e.g., Dolejš and
85 Baker, 2007b; Dolejš and Baker, 2007a). Even though more complex, substantial effects
86 on the liquidus temperature have also been reported for Cl-bearing natural melts of both
87 basaltic (e.g., Filiberto et al., 2014; Farcy et al., 2016) and silicic systems (Feisel et al.,
88 2022). The physico-chemical effects of added Br and I to a melt are, by contrast, far less
89 understood. Concentrations of Br and I are typically lower than those of F and Cl,
90 consistent with an increasing fluid-melt partition coefficient with increasing ionic radius
91 of Cl , Br and I (181, 196 and 220 pm, respectively; Bureau et al., 2000). F (133 pm)
92 instead has an ionic radius very similar to O^{2-} and OH^- (140 and 137 pm; Shannon, 1976)
93 and can therefore easily substitute for these components which promotes its solubility
94 and compatibility in the melt (Balcone-Boissard et al., 2010).
95 Volcanic halogen degassing can have significant impacts on the environment and Earth's
96 climate, for example by the depletion of stratospheric ozone by Cl and Br (Bobrowski et
97 al., 2003; Bobrowski et al., 2007; von Glasow et al., 2009; Surl et al., 2015; Roberts, 2018).
98 The degassing of F and Cl into isolated pores of slowly cooling magma was shown to cause
99 etching of silica and re-precipitation of vapor-phase cristobalite (e.g., Horwell et al., 2010;
100 Schipper et al., 2020).
101 Due to the high impacts that halogens can have on volcanological and environmental
102 processes, they have received increasing attention in recent years and are routinely

103 measured in volcanic plumes. Halogen exsolution was shown to occur at relatively
104 shallow depths compared to the release of H_2O or CO_2 (e.g., Spilliaert et al., 2006; Schipper
105 et al., 2019) and may therefore help to characterize volcanic degassing. Due to the large
106 differences in diffusivity between water and the halogens, as well as amongst halogens
107 themselves, diffusive fractionation is expected to occur during melt inclusion entrapment
108 or bubble and crystal growth (e.g., Alletti et al., 2007). Relative halogen (or halogen
109 ratios) measurements in volcanic gases and plumes could therefore be applied to track
110 diffusive fractionation processes in order to monitor volcanic activity at depth.
111 Even though halogen diffusion has been investigated since the 1980s our knowledge is
112 still far from complete. It was shown that halogen diffusion is independent of its
113 concentration and follows Arrhenian behavior in silicate melts. A weak pressure-
114 dependence on diffusivities was reported by some authors (e.g., Dingwell and Scarfe,
115 1984; Bai and Koster van Groos, 1994), however, most recent studies have found only
116 minor pressure effects (e.g., Alletti et al., 2007; Balcone-Boissard et al., 2020). Many
117 studies focused on simplified model systems (Dingwell and Scarfe, 1984; Dingwell and
118 Scarfe, 1985; Bai and Koster van Groos, 1994) and most investigated F and/or Cl only
119 (Balcone-Boissard et al., 2009; Böhm and Schmidt, 2013; Fortin et al., 2017; Yoshimura,
120 2018; Feisel et al., 2019). To date only two studies include Br diffusion (Alletti et al., 2007;
121 Balcone-Boissard et al., 2020) and, to our knowledge, no study has addressed iodine
122 diffusion.
123 In this study we applied the diffusion couple technique on three different homogeneous
124 melts synthesized from natural silicic pumice and lava to determine the diffusivity of all
125 halogens (F, Cl, Br, I) over a temperature range relevant to the studied magmatic systems.
126 Concentration profiles of F and Cl were measured by electron microprobe (EPMA) and
127 additional profiles were acquired by secondary ion mass spectrometry (SIMS) covering

all halogens. We report data for both anhydrous and hydrous (~1.5 wt.% H_2O) conditions and this is — to our knowledge — the first study to report iodine diffusion data in natural silicate melts. These results highly improve our understanding of magmatic halogen transport mechanisms at crustal conditions and expand the database of halogen diffusion to advance a thorough understanding of volcanic processes.

2. Methods

2.1 Experimental procedure

Two different starting materials were used in this study comprising glass synthesized from tephra of the Hekla (Iceland) H3 eruption (e.g., Thordarson and Larsen, 2007; Weber and Castro, 2017), and glass synthesized from natural obsidian lava of the 2011 Cordón Caulle eruption, Chile (e.g., Castro et al. 2013, 2016; Schipper et al. 2013, 2019; Alloway et al. 2015). Synthesis and experimental methods utilizing the Hekla material ("HX" series – "Hekla experiments") are described in detail in the study of Feisel et al. (2019). Synthesis of starting glass derived from Cordón Caulle obsidian lava ("CCX" series – "Cordón Caulle experiments") is described in detail in Feisel et al. (2022). The general approach used for both melts is briefly described below.

The initial sample synthesis was carried out in the laboratories of the Earth Science department of the LMU Munich. Natural obsidian was crushed, synthesized and homogenized at high temperature (1400–1550 °C) for ~2 days to produce almost completely volatile-free glass. After the first synthesis, the batch was crushed and split. One half was enriched with halogen-bearing Na-salts (NaF, NaCl, NaBr, NaI) so that each halogen would account for approximately 1 wt.% of the whole batch after mixing. The halogen-depleted split was in turn enriched with a certain amount of Na_2CO_3 to account for the sodium enrichment in the halogen-bearing glass, due to the use of aforementioned

Na-salts to add halogens. Each aliquot was again synthesized and homogenized at high T before preparation of ca. 2 mm thick polished glass discs (4.6 mm diameter) and crushed glass powder to be used in anhydrous and hydrous diffusion experiments, respectively.

2.1.1 Anhydrous diffusion experiments

Diffusion couples were constructed using 5 mm platinum tube with a wall thickness of 0.2 mm. The bottom of the capsule was closed with a Pt lid which was pressed onto and welded to the tube using an arc-welder. Afterwards the bottom of the capsule was tamped into a cylindrical shape. One halogen-enriched glass disc was loaded into the bottom of the capsule and a disc of the equivalent halogen-depleted glass was loaded on top of it, resulting in both pieces touching at their polished surfaces. Each capsule was closed by welding a second lid to the top of the capsule, which ensured closed-system conditions. The diffusion experiments were carried out in a vertical tube furnace at atmospheric pressure. Each capsule was first weighed and then loaded into an alumina tube that is closed on the bottom end, making sure the halogen-depleted half was facing upwards. After the furnace equilibrated at the target temperature the alumina tube was inserted vertically into the furnace through a small opening in the top, ensuring that the capsule was sitting upright on the closed bottom of the alumina tube in the hot zone of the furnace. The temperature was monitored by the internal thermocouple and an external K-type thermocouple being in direct contact with the experimental capsule. Additionally, most experiments were monitored using a second external K-type thermocouple interfaced with an Arduino microprocessor to read the temperature remotely and store the *P-T-t* data to a computer. Temperatures are estimated to be accurate to ±2 °C based on the manufacturer's (*Omega*) reported accuracy of the thermocouple device. The experimental durations ranged from ~20 hours to 35 days depending on the temperature

178 investigated. The time needed for the capsule to heat to the target temperature ranged
179 between 3 and 5 minutes. The experiments were quenched by sliding the alumina tube
180 out of the hot furnace and letting it cool in air at room temperature in an upright position.
181 Typical cooling times to a temperature of 200 °C as indicated by the external
182 thermocouple were in the range of 3 to 4 minutes. After each experiment the samples
183 were weighed again to confirm closed-system conditions were maintained during the
184 experiment.
185
186 *2.1.2 H_2O-bearing diffusion experiments*
187 Hydrous experiments were carried out using CCX starting material only and are denoted
188 by "CCX-H". The capsule preparation followed the procedure described in Feisel et al.
189 (2022) using powdered starting glass and Pt-tube with a diameter of 4 mm and a wall
190 thickness of 0.2 mm as capsule material. After welding the capsule shut on the bottom
191 and tamping into a cylindrical shape using a tight-fitting rod, ground glass powder of the
192 halogen-enriched samples was introduced until the capsule was filled about halfway.
193 During filling the powder was slightly tamped several times to avoid entrapment of air
194 and ensure a flat diffusion interface. The exact amount of added sample powder was
195 weighed using an analytical balance of 5-digit precision and the equivalent amount of 1.5
196 wt.% H_2O was added to the capsule using a microsyringe. The procedure was repeated
197 using the halogen-depleted powder and again the equivalent amount of 1.5 wt.% H_2O for
198 the top part of the capsule. Finally, the capsule was closed by welding a tight-fitting lid to
199 the open end and tamped into cylindrical shape with a pressure of ~750 kg using a
200 hydraulic press. Before an experiment, the capsules were repeatedly heated to ~120 °C
201 and weighed to confirm no weight loss. Capsules with significant weight loss were
202 discarded.

Experiments were performed in a *Deltech* vertical tube furnace fitted with a gas-pressurized TZM (Tungsten Zirconium Molybdenum) cold-seal pressure vessel assembly. The sample capsule is loaded into the cold-seal assembly which is connected to a stainless-steel high-pressure tubing using Argon gas as a pressure medium. To mitigate water-loss from inside the capsule to the Ar-atmosphere ca. 0.3 MPa of CH_4 was inserted to the pressure system before pressurizing with Ar (e.g., Sisson and Grove, 1993; Szramek et al., 2006; Shea and Hammer, 2013). The cold-seal assembly consists of an inner autoclave made of TZM (~30 mm outer, ~6.5 mm inner diameter) and an outer sheath made of Inconel (~50 mm diameter, 5 mm wall thickness), both attached to a water-cooled base on the bottom. The outer sheath slides over the inner autoclave leaving ~5 mm between the two. This space is constantly purged with Ar during the experiment to provide a non-reactive atmosphere for the inner pressurized autoclave. The inner autoclave is tightened against a steel cylinder via a doubly coned and sealed small Beryllium-bronze cylinder ("football"-shape) between the two. A second, lower vessel made of stainless steel is attached to the bottom of the water-cooled coupling base and is connected to the pressure line on the bottom with a high-pressure fitting. The sample capsule sits in a small cup which in turn is attached to an Inconel rod which is inserted into the bottom of the steel cylinder. A magnet at the bottom of the rod allows for the control of the position of the sample capsule in the assembly from the outside using a neodymium ring-magnet that slides over the lower steel cylinder. The whole assembly including the experimental capsule is inserted into the vertical tube furnace from the bottom before it is brought up to the target temperature and pressure. The pressure is generated by an HIP GB-60 gas booster device operated with compressed air and conveying Ar gas as a pressurizing medium.

During the time of heating, the capsule remains in the water-cooled part of the assembly (rapid-quench coupler) which is outside the furnace and constantly flushed with water (~15 l/min). When the target *P*-*T* conditions are reached and equilibrated, the experiment is started by upward movement of the sample holder using the outer magnet. In this way, the capsule is — within seconds — brought into the top part of the TZM autoclave, which is in the hot zone of the furnace. Quenching is done the opposite way by sliding the magnet down to bring the capsule back into the water-cooled zone of the assembly, resulting in an almost immediate quench. During the experiments, temperature is monitored using the internal thermocouple of the furnace and an external K-type thermocouple which is inserted into a small bore in the sheath of the TZM assembly and touching the top of the internal autoclave, which is the position closest to the capsule. The pressure is monitored with a factory-calibrated Bourdon-tube gauge and a digital pressure transducer. Considering the small thermal volume of the capsule relative to the massive TZM autoclave we expect no significant thermal gradient within the diffusion couple capsule.

Upon the start of the experiment while inserting the rod with the sample capsule into the hot zone of the autoclave, a pressure drop of up to 20 MPa over ca. 10 s is commonly observed. We interpret this to occur due to the displacement and concomitant cooling of a large amount of the hot gas from the autoclave to the cooler parts of the pressure system during to insertion of the rod. The rod is cold relative to the hot atmosphere in the autoclave and upon heating causes the pressure to increase again slowly by typically about 10 MPa over the duration of ca. 50 s. The opposite process is observed upon quench of the experiment, resulting in an up to 20 MPa overpressure during quench, which decreases to ca. 10 MPa overpressure in about 50 s at the end of an experiment. These processes are accounted for by slight over-pressurization before the start of the

253 experiment. The pressure increase at the end of the experiment also ensures that bubbles
254 do not form during the quench. Additionally, it was shown that halogen diffusion is mostly
255 insensitive to pressure variations (e.g., Baker and Balcone-Boissard, 2009). Therefore, we
256 consider these short-lived pressure fluctuations to be insignificant for the results of the
257 diffusion experiments.
258
259 **2.2 Analytical methods**
260 Before preparation for further analyses all samples were weighed individually to ensure
261 no weight loss or gain occurred during the experiment. Diffusion couple capsules were
262 embedded in epoxy and cut open along the center of the capsule and parallel to the
263 diffusion direction (i.e., parallel to the cylindrical capsules rotation axis) using a *Buehler*
264 IsoMet precision saw. All samples were polished using a series of diamond embedded
265 disks to an ultimate grain size of 1 μm while taking care that the polished surface
266 remained parallel to the diffusion direction.
267
268 *2.2.1 Electron probe micro analysis (EPMA)*
269 Major element and halogen concentration analyses of experimental glasses were
270 conducted at the Department of Geoscience of the University of Mainz, and using a *JEOL*
271 JXA8200 electron microprobe. Analyses employed an acceleration voltage of 15 kV, a
272 beam current of 12 nA, and a beam diameter of 10 μm. Dwell times for F and Cl were 120
273 s and 30 s, respectively, yielding a detection limit of 60 ppm (1 σ). Analysis dwell times
274 of each major element was: Si 25 s, Al 40 s, Na 20 s, K 30 s, Ca 30 s, Fe 60 s, Mg 30 s, Mn
275 50 s, and Ti 30 s. The device was calibrated before a measurement using the following
276 reference materials: SrF_2 (F), tugtupite (Ca, Na), VG-2 (Ca, Mg), VG-A99 (Fe, Si), MnTi (Mn,
277 Ti), and orthoclase (Al, K). Proper calibration was assessed by analyzing standards VG-2,

VG-A99, VG-568 and a natural obsidian standard (~74 wt.% SiO_2) repeatedly during each analytical session. The data was corrected using the ZAF method.

Concentration vs. distance profiles were acquired using line-scans with a fixed step-width of 5–250 µm depending on the sample (i.e., the anticipated diffusive speeds and therefore profile distances) and the position of the analyzed points relative to the diffusion interface. Points in the transition zone between the two diffusion couple halves were analyzed using a smaller step-width while the profile ends were covered by a larger step-width. This way it was possible to achieve a high spatial resolution of data, in turn facilitating good resolution of slow diffusion patterns while covering a large range of diffusion widths and keeping analysis time low. Profiles were acquired along traverses away from the capsule edges to avoid analyzing inhomogeneities that could distort diffusion profile data (e.g., devitrification, Feisel et al. 2019).

2.2.2 Secondary Ion Mass Spectrometry (SIMS)

As the concentration of Br and I in the samples is too low to be analyzed by EPMA, experimental samples were further analyzed on the SIMS. The analyses of all HX samples and of CCX1 and CCX4 were carried out during two analytical sessions in October 2018 and January 2019 at the University of Lausanne, Switzerland. The other samples (CCX3, CCX5 and all CCX-H) were analyzed at Heidelberg University, Germany, in two sessions in May 2021 and April 2022. Both facilities feature a *CAMECA* IMS 1280HR ion microprobe. The analytical parameters for all SIMS analyses (halogens and H_2O) in both labs are summarized in Table S1 of the supplementary material.

Analyses carried out at the University of Lausanne were referenced internally on each sample in an area far outside of the region of diffusion where the constant Si-content was

known from EPMA analyses. These data included the less abundant Si-isotope ^{30}Si for calculation of ratios with Br and I which are of low concentration in our samples compared to F and Cl. ^{28}Si and ^{19}F intensities were detected using a Faraday-Cup. The other halogens (^{35}Cl, $^{79/81}Br$, ^{127}I) and ^{30}Si were analyzed using electron multipliers.

The SIMS analyses of halogens in Heidelberg were calibrated using an obsidian glass (JV1, Pichavant, 1987) for F and Cl and the GSE-1G glass for Br and I (Marks et al., 2017a; Marks et al., 2017b; Wiedenbeck, 2017). The accuracy of these analyses is limited by the poor homogeneity of halogens in GSE-1G and the fact that JV1 is not an established reference material with multiple independent determinations of the concentrations. The halogen concentrations determined by SIMS must therefore be interpreted as semi-quantitative with an estimated accuracy of ≤ 50 % (relative error).

For each water-bearing sample (CCX-H), H_2O concentration profiles were acquired next to the halogen profiles using a *CAMECA* IMS3f ion microprobe at Heidelberg University. The H_2O background caused by in-situ contamination was reduced by using a LN_2-cooled metal plate in the sample chamber. The apparent H_2O concentration caused by in-situ contamination was monitored by analyzing San Carlos olivine and was < 0.01 wt.%. H_20 analyses were calibrated using JV1 as reference material. Accuracy is estimated to be < 20 % relative error.

3. Results

3.1 Chemical composition of starting materials

The major element compositions of the different starting materials as determined by microprobe analyses are compiled in Table 1. The synthesized samples reveal a similar composition, both plotting in the field of Trachyte in a TAS diagram, very close to the

328 borders to rhyolite and dacite. However, the CCX melt is slightly enriched in alkalies
329 (Na_2O, K_2O) compared to the HX melt. All samples were analyzed using line scans on the
330 microprobe not only to measure F and Cl gradients but also to validate major element
331 homogeneity over the diffusion couple (Fig. 1). Maximum absolute concentrations of F
332 are around 0.5–0.6 wt.% in the HX samples, and about 0.8–1 wt.% in the CCX samples. Cl
333 concentrations are about 0.2–0.3 wt.% in the HX samples and about 0.3–0.4 wt.% in the
334 CCX samples. Absolute Br and I concentrations were only measured for the CCX samples
335 using the SIMS at Heidelberg University. The maximum Br and I concentrations in the
336 halogen-enriched glasses of the CC melts are ~2500 ppm and ~300 ppm, respectively.
337
338 **3.2 Post-experimental diffusion couple textures**
339 During data acquisition, all diffusion couples were assessed for textural homogeneity by
340 means of backscattered electron images. Most samples comprised a clean and straight
341 diffusion interface between two homogeneous glassy areas which were particularly
342 prominent in the anhydrous samples. Some samples and mainly those of the hydrous
343 series contained minor cracks in the glass, which were interpreted to stem from the
344 relatively fast quenching rates (Fig. 2a). However, the cracks were not found to influence
345 the acquired diffusion data. Few samples underwent deformation during the experiments
346 caused by bubble formation or the onset of convection. Both phenomena were mostly
347 recognized in experiments of the water-bearing series in which the melt viscosity was
348 reduced due to the presence of water (e.g., Giordano et al. 2008) which enhanced
349 convection. These effects resulted in distorted diffusion couple geometry, and according
350 samples were discarded from further analysis. Small amounts of oxide phases (<100µm;
351 <<1 vol.%) were recognized in the halogen-bearing parts of some experiments utilizing
352 the CCX melt. These were analyzed qualitatively using EDS which showed they are

353 tungsten-oxides. This was interpreted to stem from a slight contamination of the sample
354 powder caused by using a tungsten-carbide mill for sample preparation. However, these
355 oxides are not thought to affect halogen diffusion in our experiments.
356
357 **3.3 Halogen diffusion coefficients**
358 Most concentration profiles comprise a smooth and symmetric transition between the
359 high and low halogen concentration portions of the charge, indicating that no other
360 processes than diffusion (e.g., convection) were involved (Fig. 1). Smooth and symmetric
361 profiles are recognized especially for experiments run at high temperatures. Diffusion
362 profiles of Br and I are in general shorter than those of F and Cl. However, all
363 concentration vs. distance profiles presented here yielded good results during fitting and
364 are treated as effective binary diffusion of each halogen element in the melt matrix (e.g.,
365 Zhang 2010).
366 Diffusion coefficients for each acquired concentration vs. distance profile were calculated
367 by fitting the respective data to the equation for constant one-dimensional diffusivity
368 between two semi-infinite media (Crank, 1975):

$$C(x,t) = \frac{C_{low} + C_{high}}{2} + \frac{C_{low} - C_{high}}{2} \operatorname{erf}\left(\frac{x - x_0}{2\sqrt{D\,t}}\right) \quad (1)$$

369 The parameter *C(x,t)* describes the concentration at distance *x* (m) after the experimental
370 time *t* (s). C_{low} (ppm) is the concentration of the halogen-poor, and C_{high} (ppm) the
371 concentration of the halogen-rich half-space. The term *erf* indicates the error function. x_0
372 (m) describes the position of the diffusion interface and is in this case determined
373 mathematically. The term *D* ($m^2\ s^{-1}$) is the diffusion coefficient.
374 Data fitting was performed using the nonlinear least-squares method implemented in a
375 *MatLab* script, specifically programmed for easy use with diffusion profile data. The

results obtained by this script were regularly validated by comparing to the results calculated by the commercially available curve-fitting software *CurveExpertPro*. As equation (1) is independent of absolute concentrations it was used with both, concentration data determined by EPMA and SIMS and ratios of halogen- over silica-concentration (e.g., F/Si) as determined by SIMS to calculate diffusion coefficients. All parameters of equation (1) except x and t were calculated based on the fitting algorithm. In some cases, parameters C_{low} and C_{high} were set manually to facilitate proper fitting calculations, for example where the analyzed profiles did not cover the whole length of diffusion for that particular profile. Additionally, some profiles suffered from slight distortion, caused, for example, by deformation of the capsule during quench, and resulting in asymmetrical profiles which was mainly prominent in the longest profiles of F diffusion. Where profiles were asymmetrical, each half of the diffusion profile was fitted individually using equation (1) and the results were compared to those of the complete profile. Those profiles of which the individually fitted halves yielded different diffusion coefficients larger than 0.6 orders of magnitude were discarded. F diffusion coefficients calculated on profiles where this method was applied are indicated by "*" in Table 2. Typical concentration vs. distance profiles of sample CCH-X-42 fitted with equation (1) are illustrated in Figure 2b. All measured diffusion profiles with their respective fit curves are provided in Figures S1-S4 of the supplementary material.

3.3.1 Anhydrous HX

Of the nine HX experiments presented in Feisel et al. (2019), six samples were analyzed by SIMS for the scope of this study. One concentration vs. distance profile was acquired for each of the samples, covering lengths of ~500–1000 μm. Diffusivities of F and Cl determined here agree well with the results of microprobe analyses indicating that F is

generally faster than Cl by up to 2 orders of magnitude in the investigated temperature range. *D* values are on the order of 10^{-15} to 10^{-13} m^2 s^{-1} for fluorine and 10^{-17} to 10^{-15} m^2 s^{-1} for chlorine, of which the lower and higher values each correspond to temperatures of 750 °C (HX9) and 950 °C (HX8), respectively (Table 2). Bromine and iodine diffusivities are generally lower than those of chlorine, with Br consistently being faster than I. D_{Br} ranges from 10^{-18} to 10^{-15} m^2 s^{-1} while D_I values are about half an order of magnitude smaller at the corresponding temperatures, ranging from ca. 10^{-18} to 10^{-16} m^2 s^{-1} (Table 2).

3.3.2 Anhydrous CCX

Out of seven anhydrous experiments performed using CCX melt and analyzed by EPMA, three were discarded due to textural features indicating compromised geometry. The remaining four experiments were additionally analyzed by SIMS. Diffusivities of all halogens in samples using the CCX melt are similar to those obtained for the HX melt. However, the difference between F and Cl diffusion is less pronounced in this melt composition compared to HX. Diffusion coefficients of F (D_F) range from ~10^{-14} to 10^{-13} m^2 s^{-1} in the temperature range of 850 °C (CCX3) to 1000 °C (CCX5). Cl diffusion is up to two orders of magnitude slower with ~10^{-17} to 10^{-14} m^2 s^{-1} at these temperatures. For these two halogens, results of EPMA and SIMS analyses agree well within statistical errors (Table 2). Diffusion of Br is slower than that of Cl by ~0.5–1.5 orders of magnitude and I is even slower than Br by ~1 order of magnitude with diffusivities in the range of ~10^{-16}–10^{-14} and ~10^{-16}–10^{-15} m^2 s^{-1}, respectively.

3.3.3 Hydrous CCX-H

All diffusion couple experiments of the hydrous series performed in the TZM assembly were analyzed both by EPMA (F, Cl) and by SIMS (F, Cl, Br, I). In general, diffusivities are higher than those obtained for the anhydrous CCX series with D_F ranging from $\sim 10^{-12}$ to $\sim 10^{-11}$ m^2 s^{-1} from 1000–1200 °C. Cl diffusion is 0.5 to 1 orders of magnitude slower than F, and Br and I are even slower. However, diffusivities of Cl, Br and I are all within less than one order of magnitude of each other at the respective experimental temperatures (Table 2). This results in a total diffusivity range of only 1–2 orders of magnitude among all halogens which is significantly less than observed for the anhydrous series of CCX melt which spans a range of 3–4 orders of magnitude among all halogens (Table 2).

3.4 Temperature dependence of halogen diffusion

All diffusion coefficients determined in this study increase with increasing temperature for each of the used melt compositions. As shown in various previous studies, diffusivity follows Arrhenian behavior (e.g., Baker and Balcone-Boissard 2009), which is also confirmed by our data. Plotted in a diagram of log(D) vs. inverse temperature (Fig. 3), the data clearly shows this Arrhenian trend and can be described by the following equation:

$$D = D_0 * e^{-\frac{E_A}{R*T}} \quad (2)$$

where D is the diffusion coefficient (m^2 s^{-1}), D_0 is the pre-exponential factor, E_A the activation energy (J/mol), R the universal gas constant (8.3145 J mol^{-1} K^{-1}), and T is the temperature (K). The characteristic parameters describing the diffusive behavior of each halogen in a specific melt composition are D_0 and E_A which are mathematically represented by the y-axis intersect and the slope of the trendline in the Arrhenius diagram, respectively. For the calculation of the characteristic Arrhenius parameters, equation (2) was linearized to the form

$$\log(D) = -\frac{E_A}{\ln(10) * R * T} + \log(D_0) \quad (3)$$

and fitted to all available data (EPMA + SIMS) of each starting material using the nonlinear least-squares method implemented with *Matlab*. Where multiple profiles were measured on one sample and with the same method, the resulting diffusion coefficients were averaged to avoid a weighing effect during the Arrhenius fitting calculations. The results of all fits are illustrated in Fig. 3 and listed in Table 3. Fitted with the data of the two anhydrous series, the results of the HX and CCX starting materials are similar, yielding activation energies in the range of ~200–290 kJ/mol for all halogens. However, diffusion in HX melt generally comprises slightly higher activation energies than in CCX melt. The similarity is further represented by the parallel fit curves in the Arrhenius diagrams (Fig. 3). However, in the HX series it is apparent that F is significantly faster than all other halogens which is represented by a gap of 1.5–2 orders of magnitude between the fit lines of F and Cl, while Cl, Br and I are all within about 1.5 orders of magnitude. In comparison, the data of the CCX series shows more equally spaced Arrhenius fits of the halogens spanning an overall similar range of diffusivities compared to the HX experiments.

The data of the hydrous series shows the same ordering of diffusive speeds, with F being the fastest and I being the slowest, but spanning a narrower range of diffusivities among all halogens. In the Arrhenius diagram this is represented by the more closely spaced fit curves compared to the anhydrous data. Activation energies are similar to the anhydrous series, except for F whose E_A is only 131 kJ/mol in the hydrous case compared to 198–213 kJ/mol in the anhydrous experiments (Table 3).

3.5 H_2O content in CCX-H experiments

The experimental products of the CCX-H series show a range of 1.5–2 wt.% H_2O (Table 2). Most of the hydrous experiments suffered from water loss to some extent, which was indicated by increasing totals towards one end of the diffusion profile recognized in the EPMA results (Fig. 1) and confirmed by SIMS analyses (Fig. 2; Fig. S1 of the supplementary material). The use of CH_4 in the pressure medium helped to reduce this issue but did not resolve it completely. Interestingly, water was only lost on the halogen-depleted side of the diffusion couple leading to a weak, mostly linear H_2O-concentration gradient over the length of the diffusion couple. Experiments comprising significant water loss were discarded, however, small losses were considered negligible with regard to diffusivity. This is particularly true considering that the transition between high and low halogen concentration in most cases is relatively narrow, especially relative to the short diffusion lengths of the slower diffusing halogens. Over this narrow range the H_2O concentration can be considered to be constant within error. Due to this issue, we have calculated the average H_2O-concentration over the length of the transition zone of each hydrous diffusion profile and reported it with other relevant data in Table 2.

4. Discussion

4.1 Halogen diffusion mechanisms

Diffusivity and the mechanism of halogen diffusion are both strongly dependent on the composition and internal structure of the host glass. In the case of aluminosilicate melts a vast range of compositions are present in nature and structural melt parameters such as the degree of polymerization show an accordingly wide range. Arrhenius parameters of halogen diffusion have been determined for a range of different melt compositions and illustrate the strong compositional dependence of halogen diffusion (Watson and Bender,

1980; Dingwell and Scarfe, 1984; Dingwell and Scarfe, 1985; Bai and Koster van Groos, 1994; Alletti et al., 2007; Balcone-Boissard et al., 2009; Böhm and Schmidt, 2013; Fortin et al., 2017; Yoshimura, 2018; Balcone-Boissard et al., 2020). Most of these studies studied F and Cl diffusion and only few have investigated Br diffusion. However, none of the available studies provide I diffusivity data. Hence the present study is the first to our knowledge.

One major compositional parameter defining the behavior of silicate melts is the degree of polymerization, which itself is a function of, for example, the amounts of SiO_2, volatiles or network modifying cations. Typically, the degree of polymerization in a melt is characterized by the parameter of NBO/T, i.e., the ratio of non-bridging oxygen atoms over tetrahedally coordinated ions (Mysen, 1988). The melts of the present study exhibit NBO/T values in the range of ~ 0.08–0.11, calculated using the method of (Mysen, 1988) and splitting FeO_{tot} equally between Fe_2O_3 and FeO (Giordano et al., 2008). The NBO/T values are reported together with the bulk rock chemistry in Table 1.

The bond strength of an ionic species dissolved in melt generally increases with the charge of that species (Zhang et al., 2010). Halogens in the combined state (e.g., as a halide) typically have an univalent charge of -1 and are therefore comparably weakly bonded to other atoms, despite being very reactive. This means that halogens are relatively easily detached from their original site by breakage of the ionic bonds around a previously coordinated halogen ion before moving to a new site (Zhang et al., 2010). Additionally, even though the halogen group elements have the highest electronegativity of all elements in their respective periods, the significant within group variation in this parameter means that the bond strength should also vary accordingly. For example, F, being the most electronegative, should foster the highest bond strength of the halogens.

Within this simplified chemical framework the diffusive "jump" can be envisioned to proceed by passing through an aperture formed by neighboring ions. The size and stiffness of the aperture should generally be structurally controlled and relate to the polymerization of the melt, while the detachment rate should be controlled by ionic charge (Zhang et al., 2010). The size and number of the apertures are determined by the ions present in the melt and the resulting "free space" formed which is called the ionic porosity. Naturally, smaller ions such as F diffuse faster, because they can pass through apertures of various sizes and are therefore less sensitive to ionic porosity. Larger ions can only pass large apertures and their diffusion-rate is therefore structurally controlled and, hence, more sensitive to ionic porosity. This is typically the case for noble gases and monovalent ions (e.g., Henderson et al., 1985; Lux, 1987; Alletti et al., 2007) and was also confirmed for halogens by recent studies which showed that diffusion is negatively correlated with the ionic radius of the halogen in low NBO/T melts, i.e., in melts with a high degree of polymerization (Rhyodacite/Trachyte, NBO/T: ~0.08, Feisel et al., 2019; Na- and K-Phonolite, NBO/T: ~0.08, Balcone-Boissard et al., 2020). In melts with higher NBO/T (lower degree of polymerization) halogen diffusion typically comprises only weak correlation with the ionic radius. Alletti et al. (2007) suggested that halogen diffusion in a basaltic melt (NBO/T ~0.5) is mostly independent of "free space" in the melt structure but instead occurs by exchange mechanisms that are predominantly controlled by the preservation of local charge balance, similar to the diffusion of divalent and trivalent cations (Henderson et al., 1985). This means that in this kind of melt movement of halogens is mainly rate-limited by the charge-controlled detachment process.

The present study complements the data of Feisel et al. (2019) by including all new SIMS analyses which also cover Br and I in two different highly polymerized melts (HX: NBO/T

545 ~0.08; CCX: NBO/T ~0.08–0.11). Figure 4 illustrates the diffusivity of the halogens in
546 different melt compositions relative to their ionic radii (Shannon, 1976) at 1250 °C. The
547 data of Alletti et al. (2007) are included as a reference of a weakly polymerized melt and
548 the data of studies performed at lower temperatures were calculated based on the
549 published Arrhenius parameters. The results of the present study and especially those of
550 Br and I confirm the strong influence of the ionic radius on diffusivity in polymerized
551 anhydrous melts. The difference between F and Cl is particularly pronounced for most
552 anhydrous studies, yielding a significant negative slope between the two in the diagram
553 (Fig. 4). However, the slope between Cl and Br defines a discordance to the trend between
554 F and Cl in most studies. For the anhydrous CCX melt the slope increases from Cl to Br
555 and this trend is continued to I. For the anhydrous HX melt, however, the slope decreases
556 from Cl to Br and I. This stepwise correlation of ionic radius and diffusivity is recognized
557 for all polymerized melts that were analyzed for Br (and I). We interpret this behavior to
558 show that the ionic porosity of the melt is limited to distinct aperture sizes dictated by
559 the melt structure. The fact that Cl and Br seem to have a similar diffusivity in anhydrous
560 phonolite (Balcone-Boissard et al., 2009) regardless of their different ionic radii suggests
561 that Cl and Br move through similarly sized apertures in this melt. By contrast, in the HX
562 and especially CCX melt, Br cannot move through the same apertures as Cl due to its size,
563 resulting in its lower diffusivity. Likewise, the I ion is too large to pass these aperture
564 sizes and can diffuse only in the vicinity of ions that allow the formation of larger openings
565 between sites. F, being the fastest diffuser among all of the halogens, can move through
566 both small openings and all the larger apertures that are used by Cl, Br, and I in a
567 polymerized anhydrous melt.
568
569 **4.2 The effect of H_2O on diffusion**

570 The hydrous experiments (~1.5 wt.% H_2O) generally yield high diffusivities which span
571 a range of only 1–2 orders of magnitude among the different halogens (Fig. 3). This
572 restricted range of diffusivities contrasts those of the anhydrous CCX melt which displays
573 3–4 orders of magnitude variation. For better comparison to the anhydrous results, the
574 Arrhenius parameters of the anhydrous CCX series were used to calculate hypothetical
575 anhydrous diffusivities in the temperature range of the hydrous experiments and plotted
576 in an Arrhenius diagram together with the hydrous Arrhenius fits (Fig. 5). The calculated
577 anhydrous values are consistently lower than the hydrous data. While the difference for
578 F is only ~0.2 log units at high T (1200 °C) and ~0.8 log units at low T (1000 °C), the
579 difference for the slower diffusing halogens is more pronounced. Cl is ~1 log unit, Br
580 ~0.5–1.5 log units and I ~2 log units faster in hydrous compared to dry melt. These
581 results highlight the strong influence of H_2O on halogen diffusivity in the high silica melts
582 of this study. These findings are in contrast to the those of Balcone-Boissard et al., (2020),
583 who showed that the addition of up to 2.65 wt.% H_2O exerts only minor influence on Br
584 diffusion in phonolitic melts; a fact which further underlines the strong compositional
585 dependence of halogen diffusion.
586
587 The increase in diffusivity in the melts of this study indicates a change in the diffusion
588 mechanism that is likely caused by the modification of the melt structure due to the
589 addition of H_2O. This effect can also be observed in Figure 4, where the strong correlation
590 of diffusivity with the ionic radii observed in the anhydrous melts is highly attenuated for
591 the hydrous case. Indeed, the hydrous data is more similar to those of basalt confirming
592 that water effectively lowers the degree of polymerization of the melt. In doing so, the
593 rate-limiting influence of melt structural apertures is reduced which makes the process
594 of detachment more relevant as a diffusion-rate-limiting factor. Interestingly, the slope

595 between Cl and Br increases in the hydrous melt similar to the behavior in the anhydrous
596 CCX melt. At the relatively low water contents of ~1.5 wt.% used in the present study, the
597 majority of the added H_2O is expected to be dissociated to form hydroxyl (OH) in the melt
598 (e.g., Silver et al., 1990; Ihinger et al., 1999). The experimental results indirectly show that
599 hydroxyl effectively depolymerizes the melt and allows for faster halogen diffusion.
600 However, even in the hydrated melt, halogen diffusion is still somewhat correlated with
601 the ionic radii. This may indicate that for the given added water content (~1.5 wt.%) the
602 melt structure is still polymerized enough to assert some control on the aperture-limited
603 jumping processes, mainly affecting larger ions. We speculate that diffusivities will
604 increase even more and may become more equal among the halogen species with
605 increased water content. Indeed, our own preliminary results using 3.5 wt.% of H_2O
606 added to the same CCX melt and in the same experimental setup (e.g., 1000 °C / 160 MPa)
607 yield still higher diffusivities that span over an even smaller range among all the halogens
608 (Fig. 5). This strongly implies that the rate at which a halogen ion jumps into a new site
609 grows as the melt becomes increasingly depolymerized.
610
611 Another notable distinction between anhydrous and hydrous melt is the change in the
612 activation energy, E_A, of F diffusion, which is lowered from 198 to 131 kJ mol^{-1}, while the
613 E_A of the other halogens are only weakly affected (Table 3). That is, F diffusion becomes
614 less sensitive to temperature in hydrous melts, which is apparent in the comparably
615 shallow slope of the F Arrhenius fit in Figures 3c and 5. As already concluded from the
616 observation that F diffusion is less strongly enhanced in the hydrous melt, compared to
617 the other halogens, F diffusion appears only weakly sensitive to the melt structure and is
618 more strongly controlled by the detachment process. F is known to substitute for bridging
619 oxygen in Si-O-Si units (e.g., Mysen and Virgo, 1985) and preferably coordinates with Si

620 or Al (e.g., Zeng and Stebbins, 2000; Liu and Nekvasil, 2002) , while Cl and Br prefer to
621 coordinate in larger sites (Cassidy et al., *in press*). Similarly, OH^- typically replaces oxygen
622 bonds of the Si-O network (Mysen et al., 1980). Consequently, the addition of H_2O and the
623 concomitant formation of OH^- in the melt must influence the preferred bonding
624 environment of F in the silicate network. Here, we interpret the change in activation
625 energy of F to reflect that the rate of detachment from its site is enhanced by the
626 replacement of F with OH^-. This way more F is available for diffusion compared to the
627 anhydrous case, which in turn suggests that F diffusion becomes less sensitive to
628 temperature (i.e., lower activation energy) under hydrous conditions. Consequently, we
629 speculate that the introduction of water has a two-fold effect on the halogen diffusion
630 mechanism: 1) The resulting decrease in the degree of polymerization generally
631 promotes halogen diffusivities by increasing the ionic porosity; 2) The strong effect on
632 the activation energy of F is interpreted to be due to OH^- directly affecting the bonding
633 environment of F. Clearly, these explanations are qualitative, and therefore meant to
634 suggest possible microscale chemical processes that might explain our macroscopic
635 observations. Testing these ideas could benefit from appropriate imaging experiments
636 (e.g., Schaller et al., 1992; Zeng and Stebbins, 2000; Mysen et al., 2004) that may isolate
637 the relevant coordination and bonding environments of the halogens, with implications
638 for their bond strengths in natural silicate melt.
639

640 **4.3 Halogen diffusion and viscosity**

641 Oxygen self-diffusion is commonly seen as a solid estimate of the structurally defined
642 lower limit of diffusion rates in silicate melts (Oishi et al., 1975; Shimizu and Kushiro,
643 1984; Dingwell, 1990; Lesher, 2010; Zhang and Ni, 2010) and appears closely related to
644 anhydrous melt viscosity via the Eyring equation (Glasstone et al., 1941; Dingwell, 1990;

645 Zhang and Ni, 2010). Calculated oxygen self-diffusivity of our anhydrous samples using
646 viscosity data derived from the model of Giordano et al. (2008) are included in Figure 3.
647 Diffusion of all four halogens in the dry melt is at least 1 order of magnitude faster than
648 the calculated oxygen self-diffusion (Fig. 3), indicating that the silicate network behaves
649 as in quasi-static structural sites relative to the diffusing halogen ion; therefore, diffusion
650 may only be affected weakly by self-diffusion of the silicate network. Notably, iodine
651 diffusion is the slowest of the halogens and thus closest to the calculated Eyring diffusion.
652 The steeper slope of the Eyring diffusivity compared to the slope of the halogen fits in the
653 Arrhenius diagrams (Fig. 3) suggests that with increasing temperature the jump
654 frequency of iodine may approach that of the Si-O bonds in the silicate structure and the
655 network surrounding iodine may no longer be viewed as quasi-static. With increasing
656 temperature, iodine diffusion might therefore be enhanced by the cooperative
657 rearrangement of the local silicate structure as oxygen diffuses.
658 The activation energy of diffusion, i.e., the slopes of the Arrhenius fits of the other
659 halogens (Fig. 3) likewise indicate that all fits will meet the lower limit of oxygen self-
660 diffusion at higher temperatures. Consequently, at sufficiently high temperatures (i.e.,
661 sufficiently low viscosity), all halogens will move with the same frequency as the silicate
662 network, hence, diffusion will be the same for all halogens, being determined by the jump
663 frequency of the structural movement of the Si-O bonds, broadly consistent with the
664 conclusions of Dingwell (1990).
665 The indicated oxygen self-diffusivities in Figure 3 are considered to represent the lower
666 limit of possible values as they are based on the halogen-depleted melt compositions. In
667 F bearing melts, like those of the enriched diffusion couple halves, the viscosity can be
668 significantly reduced due to the depolymerizing effect of F (e.g., Dingwell et al., 1985;
669 Giordano et al., 2008), which will in turn yield higher calculated oxygen self-diffusivities.

For the melts used in this study, the F-bearing melts yield Eyring diffusivities of up to 1 order of magnitude higher than the F-depleted melts, approaching the derived diffusivities of iodine at the highest of the experimental temperatures. Therefore, during the experiments, the melt structural lower limit of halogen diffusion is expected to change upon diffusion of F. In the resulting F enriched melts, the halogen diffusivities might approach the Si-O jump frequency already at lower temperatures compared to the F-depleted case. Expanding on this idea, we speculate that when F diffusivity and the F-depleted Eyring diffusivity are within ~1 order of magnitude in Arrhenius space (i.e., at sufficiently high temperatures), diffusion of F into the depleted melt will enhance F diffusivity by decreasing the degree of polymerization. This would in turn result in a concentration dependent F diffusivity comparable to the case of H_2O (e.g., Behrens et al., 2004). However, it is unclear if the Eyring equation is valid for the case of F-enriched polymerized melts.

In case of the hydrous melt, the Eyring equation was shown to be inapplicable as it under-estimates oxygen-diffusion by 3–4 orders of magnitude in rhyolitic melt (Behrens et al., 2007). In this case, oxygen no longer moves solely by self-diffusion but is mainly transported by the diffusion of molecular H_2O in the melt (Behrens et al., 2007; Zhang and Ni, 2010) which shows that the structural limit of diffusion rates in hydrous melt can no longer be described by the self-diffusion of oxygen.

In an attempt to define a lower limit of diffusion rates in the hydrous melt of the present study, calculated oxygen self-diffusivities of rhyolite and dacite (Tables 4 and 5 of Zhang and Ni, (2010)) have been included in Figure 3c. However, these predicted self-diffusivities are faster than the experimentally constrained diffusivities of Br and I over a large range of the investigated temperatures. This is interpreted to indicate that in a

695 slightly depolymerized melt of sufficiently large ionic porosity, the jumps of Si-O bonds
696 no longer define the lower limit of transport rates but that the diffusive characteristics
697 may be mostly determined by the ionic charge and radius.
698
699 **5. Conclusions**
700 The diffusion characteristics of four halogens in silicic melts were determined
701 experimentally under anhydrous and hydrous conditions and over a temperature range
702 relevant for magmatic processes (750–1200 °C). The results are consistent in that F is the
703 fastest diffusing halogen and diffusivity decreases with increasing ionic radius indicating
704 that diffusivity is highly dependent on the melt structure and therefore melt composition.
705 Halogen diffusion covers a range of 3–4 orders of magnitude in silica-rich anhydrous
706 melt, but diffusivities increase dramatically when water is added. The diffusivity increase
707 due to the addition of water is most pronounced for the largest of the halogens and thus,
708 the slowest diffusing halogen iodine. The effect of added water is weaker for the smaller
709 halogens, leading to an overall diffusive range of only 1–2 orders of magnitude among all
710 halogens. While the temperature dependence in terms of activation energies of Cl, Br and
711 I diffusion is similar in the dry and wet case (~200–290 kJ/mol), E_A of F is reduced by
712 about 35% in hydrous (~131 kJ/mol) compared to anhydrous melt (~200 kJ/mol). This
713 is interpreted to indicate that F diffusion is more strongly dependent on the ionic
714 detachment during diffusion and is therefore less sensitive to ionic porosity, especially in
715 hydrous melt.
716 This study represents a significant contribution to the experimental database of halogen
717 diffusion in natural silicate melts, and to our knowledge, is the first to include coherent
718 results on iodine diffusion. The new data are highly relevant for the better understanding
719 of halogen mobility in magmatic processes. Our results suggest that diffusive

fractionation of faster diffusing components such as H_2O and the halogens, could occur during bubble formation in a weakly water-enriched magma during slow magma ascent (e.g., Watson, 2017). Modeling of different magma ascent and bubble growth scenarios using the proposed diffusion parameters may help to characterize possible halogen fractionation trends during volcanic unrest.

Acknowledgements

We thank N. Groschopf and S. Buhre for their guidance during electron microprobe analyses. T. Häger is thanked for access to the precision diamond wire saw. The help of B. Scheu, U. Kueppers, and K.-U. Hess with pre-synthesis sample preparation at LMU Munich is appreciated. This research was part of the Ph.D. thesis of Y. Feisel at the Johannes Gutenberg-University, Mainz. It was supported by a fellowship of the Gutenberg Research College of the Johannes Gutenberg-University of Mainz to D.B. Dingwell, who also acknowledges the support of ERC2018 ADV Grant 834225 (EAVESDROP).

REFERENCES

Aiuppa A., Baker D. R. and Webster J. D. (2009) Halogens in volcanic systems. *Chem. Geol.* **263**, 1–18.

Alletti M., Baker D. R. and Freda C. (2007) Halogen diffusion in a basaltic melt. *Geochim. Cosmochim. Acta* **71**, 3570–3580.

Alloway B. V., Pearce N. J. G., Villarosa G., Outes V. and Moreno P. I. (2015) Multiple melt bodies fed the AD 2011 eruption of Puyehue-Cordón Caulle, Chile. *Sci. Rep.* **5**, 1–8.

Baasner A., Schmidt B. C. and Webb S. L. (2013) Compositional dependence of the rheology of halogen (F, Cl) bearing aluminosilicate melts. *Chem. Geol.* **346**, 172–183.

Bai T. B. and Koster van Groos A. F. (1994) Diffusion of chlorine in granitic melts. *Geochim. Cosmochim. Acta* **58**, 113–123.

746 Baker D. R. and Balcone-Boissard H. (2009) Halogen diffusion in magmatic systems: Our current
747 state of knowledge. *Chem. Geol.* **263**, 82–88.
748 Balcone-Boissard H., Baker D. R., Villemant B. and Boudon G. (2009) F and Cl diffusion in
749 phonolitic melts: Influence of the Na/K ratio. *Chem. Geol.* **263**, 89–98.
750 Balcone-Boissard H., Baker D. R., Villemant B., Cauzid J., Boudon G. and Deloule E. (2020) Br
751 diffusion in phonolitic melts: Comparison with fluorine and chlorine diffusion. *Am. Mineral.*
752 **105**, 1639–1646.
753 Balcone-Boissard H., Villemant B. and Boudon G. (2010) Behavior of halogens during the
754 degassing of felsic magmas. *Geochemistry, Geophys. Geosystems* **11**.
755 Behrens H., Zhang Y., Leschik M., Wiedenbeck M., Heide G. and Frischat G. H. (2007) Molecular
756 H_2O as carrier for oxygen diffusion in hydrous silicate melts. *Earth Planet. Sci. Lett.* **254**,
757 69–76.
758 Behrens H., Zhang Y. and Xu Z. (2004) H_2O diffusion in dacitic and andesitic melts. *Geochim.*
759 *Cosmochim. Acta* **68**, 5139–5150.
760 Bobrowski N., von Glasow R., Aiuppa A., Inguaggiato S., Louban I., Ibrahim O. W. and Platt U.
761 (2007) Reactive halogen chemistry in volcanic plumes. *J. Geophys. Res. Atmos.* **112**.
762 Bobrowski N., Hönninger G., Galle B. and Platt U. (2003) Detection of bromine monoxide in a
763 volcanic plume. *Nature* **423**, 273–276.
764 Böhm A. and Schmidt B. C. (2013) Fluorine and chlorine diffusion in phonolitic melt. *Chem. Geol.*
765 **346**, 162–171.
766 Bureau H., Keppler H. and Métrich N. (2000) Volcanic degassing of bromine and iodine:
767 Experimental fluid/melt partitioning data and applications to stratospheric chemistry.
768 *Earth Planet. Sci. Lett.* **183**, 51–60.
769 Cassidy M., Iveson A. A., Humphreys M. C. S., Mather T. A., Helo C., Castro J. M., Ruprecht P., Pyle
770 D. M. and EIMF (2022) Experimentally-derived F, Cl, and Br fluid/melt partitioning of
771 intermediate to silicic melts in shallow magmatic systems. *Am. Mineral.*
772 doi.org/10.2138/am-2022-8109

773 Castro J. M., Cordonnier B., Schipper C. I., Tuffen H., Baumann T. S. and Feisel Y. (2016) Rapid
774 laccolith intrusion driven by explosive volcanic eruption. *Nat. Commun.* **7**, 13585.
775 Castro J. M., Schipper C. I., Mueller S. P., Militzer A. S., Amigo A., Parejas C. S. and Jacob D. (2013)
776 Storage and eruption of near-liquidus rhyolite magma at Cordón Caulle, Chile. *Bull.*
777 *Volcanol.* **75**, 1–17.
778 Crank J. (1975) *The Mathematics of Diffusion*., Clarendon-Oxford, London.
779 Dingwell D. B. (1990) Effects of structural relaxation on cationic tracer diffusion in silicate
780 melts. *Chem. Geol.* **82**, 209–216.
781 Dingwell D. B. and Hess K. U. (1998) Melt viscosities in the system Na-Fe-Si-O-F-Cl; contrasting
782 effects of F and Cl in alkaline melts. *Am. Mineral.* **83**, 1016–1021.
783 Dingwell D. B. and Scarfe C. M. (1984) Chemical diffusion of fluorine in jadeite melt at high
784 pressure. *Geochim. Cosmochim. Acta* **48**, 2517–2525.
785 Dingwell D. B. and Scarfe C. M. (1985) Chemical diffusion of fluorine in melts in the system
786 Na_2O-Al_2O_3-SiO_2. *Earth Planet. Sci. Lett.* **73**, 377–384.
787 Dingwell D. B., Scarfe C. M. and Cronin D. J. (1985) The effect of fluorine on viscosities in the
788 system Na_2O - Al_2O_3 - SiO_2: implications for phonolites, trachytes and rhyolites. *Am.*
789 *Mineral.* **70**, 80–87.
790 Dolejš D. and Baker D. R. (2007a) Liquidus equilibria in the system K_2O-Na_2O-Al_2O_3-SiO_2-F_2O_{-1}-
791 H_2O to 100 MPa: I. Silicate-fluoride liquid immiscibility in anhydrous systems. *J. Petrol.* **48**,
792 785–806.
793 Dolejš D. and Baker D. R. (2007b) Liquidus equilibria in the system K_2O-Na_2O-Al_2O_3-SiO_2-F_2O_{-1}-
794 H_2O to 100 MPa: II. Differentiation paths of fluorosilicic magmas in hydrous systems. *J.*
795 *Petrol.* **48**, 807–828.
796 Dolejš D. and Zajacz Z. (2018) Halogens in Silicic Magmas and Their Hydrothermal Systems. In
797 *The Role of Halogens in Terrestrial and Extraterrestrial Geochemical Processes* (eds. D. E.
798 Harlov and L. Y. Aranovich). Springer-Verlag, Cham. pp. 431–543.
799 Farcy B. J., Gross J., Carpenter P., Hicks J. and Filiberto J. (2016) Effect of chlorine on near-

liquidus crystallization of olivine-phyric shergottite NWA 6234 at 1 GPa: Implication for volatile-induced melting of the Martian mantle. *Meteorit. Planet. Sci.* **51**, 2011–2022.

Feisel Y., Castro J. M. and Dingwell D. B. (2019) Diffusion of F and Cl in dry rhyodacitic melt. *Am. Mineral.* **104**, 1689–1699.

Feisel Y., Castro J. M., Helo C. and Dingwell D. B. (2022) The effect of halogens (F, Cl) on the near-liquidus crystallinity of a hydrous trachyte melt. *Am. Mineral.* **107**, 1007–1017.

Filiberto J., Dasgupta R., Gross J. and Treiman A. H. (2014) Effect of chlorine on near-liquidus phase equilibria of an Fe-Mg-rich tholeiitic basalt. *Contrib. to Mineral. Petrol.* **168**, 1–13.

Filiberto J., Wood J., Dasgupta R., Shimizu N., Le L. and Treiman A. H. (2012) Effect of fluorine on near-liquidus phase equilibria of an Fe-Mg rich basalt. *Chem. Geol.* **312–313**, 118–126.

Fortin M. A., Watson E. B. and Stern R. (2017) The isotope mass effect on chlorine diffusion in dacite melt, with implications for fractionation during bubble growth. *Earth Planet. Sci. Lett.* **480**, 15–24.

Giordano D., Russell J. K. and Dingwell D. B. (2008) Viscosity of magmatic liquids: A model. *Earth Planet. Sci. Lett.* **271**, 123–134.

von Glasow R., Bobrowski N. and Kern C. (2009) The effects of volcanic eruptions on atmospheric chemistry. *Chem. Geol.* **263**, 131–142.

Glasstone S., Laidler K. J. and Eyring H. (1941) *The Theory of Rate Processes*., McGraw-Hill, New York.

Henderson P., Nolan J., Cunningham G. C. and Lowry R. K. (1985) Structural controls and mechanisms of diffusion in natural silicate melts. *Contrib. to Mineral. Petrol.* **89**, 263–272.

Horwell C. J., Le Blond J. S., Michnowicz S. A. K. and Cressey G. (2010) Cristobalite in a rhyolitic lava dome: Evolution of ash hazard. *Bull. Volcanol.* **72**, 249–253.

Ihinger P. D., Zhang Y. and Stolper E. M. (1999) The speciation of dissolved water in rhyolitic melt. *Geochim. Cosmochim. Acta* **63**, 3567–3578.

Lesher C. E. (2010) Self-diffusion in silicate melts: Theory, observations and applications to magmatic systems. *Rev. Mineral. Geochemistry* **72**, 269–309.

827 Liu Y. and Nekvasil H. (2002) Si-F bonding in aluminosilicate glasses: Inferences from ab initio
828 NMR calculations. *Am. Mineral.* **87**, 339–346.
829 Lux G. (1987) The behavior of noble gases in silicate liquids: Solution, diffusion, bubbles and
830 surface effects, with applications to natural samples. *Geochim. Cosmochim. Acta* **51**, 1549–
831 1560.
832 Manning D. A. C. (1981) The effect of fluorine on liquidus phase relationships in the system Qz-
833 Ab-Or with excess water at 1 kB. *Contrib. to Mineral. Petrol.* **76**, 206–215.
834 Marks M. A. W., Kendrick M. A., Eby G. N., Zack T. and Wenzel T. (2017a) The F, Cl, Br and I
835 Contents of Reference Glasses BHVO-2G, BIR-1G, BCR-2G, GSD-1G, GSE-1G, NIST SRM 610
836 and NIST SRM 612. *Geostand. Geoanalytical Res.* **41**, 107–122.
837 Marks M. A. W., Kendrick M. A., Wenzel T., Eby G. N. and Zack T. (2017b) Reply to 'Comment on
838 The F, Cl, Br and I Contents of Reference Glasses BHVO-2G, BIR-1G, BCR-2G, GSD-1G, GSE-
839 1G, NIST SRM 610 and NIST SRM 612.' *Geostand. Geoanalytical Res.* **41**, 475–478.
840 Mysen B. O. (1988) *Structure and Properties of Silicate Melts*., Elsevier, Amsterdam.
841 Mysen B. O., Cody G. D. and Smith A. (2004) Solubility mechanisms of fluorine in peralkaline and
842 meta-aluminous silicate glasses and in melts to magmatic temperatures. *Geochim.*
843 *Cosmochim. Acta* **68**, 2745–2769.
844 Mysen B. O. and Virgo D. (1985) Interaction between fluorine and silica in quenched melts on
845 the joins SiO_2-AlF_3 and SiO_2-NaF determined by raman spectroscopy. *Phys. Chem. Miner.* **12**,
846 77–85.
847 Mysen B. O., Virgo D., Harrison W. J. and Scarfe C. M. (1980) Solubility mechanisms of H_2O in
848 silicate melts at high pressures and temperatures: a Raman spectroscopic study:
849 discussion. *Am. Mineral.* **65**, 900–914.
850 Oishi Y., Terai R. and Ueda H. (1975) Oxygen Diffusion in Liquid Silicates and Relation to their
851 Viscosity. In *Mass Transport Phenomena in Ceramics* pp. 297–310.
852 Pichavant M. (1987) The Macusani glasses, SE Peru: evidence of chemical fractionation in
853 peraluminous magmas. *Magmat. Process. Physicochem. Princ.*, 359–373.

Roberts T. (2018) Ozone Depletion in Tropospheric Volcanic Plumes: From Halogen-Poor to Halogen-Rich Emissions. *Geosciences* **8**, 68.

Schaller T., Dingwell D. B., Keppler H., Knöller W., Merwin L. and Sebald A. (1992) Fluorine in silicate glasses: A multinuclear magnetic resonance study. *Geochim. Cosmochim. Acta* **56**, 701–707.

Schipper C. I., Castro J., Kennedy B., Christenson B., Aiuppa A., Alloway B., Forte P., Seropian G. and Tuffen H. (2019) Halogen (Cl, F) release during explosive, effusive, and intrusive phases of the 2011 rhyolitic eruption at Cordón Caulle volcano (Chile). *Volcanica* **2**, 73–90.

Schipper C. I., Castro J. M., Tuffen H., James M. R. and How P. (2013) Shallow vent architecture during hybrid explosive-effusive activity at Cordón Caulle (Chile, 2011-12): Evidence from direct observations and pyroclast textures. *J. Volcanol. Geotherm. Res.* **262**, 25–37.

Schipper C. I., Rickard W. D. A., Reddy S. M., Saxey D. W., Castro J. M., Fougerouse D., Quadir Z., Conway C., Prior D. J. and Lilly K. (2020) Volcanic SiO_2-cristobalite: A natural product of chemical vapor deposition. *Am. Mineral.* **105**, 510–524.

Shannon R. D. (1976) Revised effective ionic radii and systematic studies of interatomic distances in halides and chalcogenides. *Acta Crystallogr. Sect. A* **32**, 751–767.

Shea T. and Hammer J. E. (2013) Oxidation in CSPV experiments involving H_2O-bearing mafic magmas: Quantification and mitigation. *Am. Mineral.* **98**, 1285–1296.

Shimizu N. and Kushiro I. (1984) Diffusivity of oxygen in jadeite and diopside melts at high pressures. *Geochim. Cosmochim. Acta* **48**, 1295–1303.

Silver L. A., Ihinger P. D. and Stolper E. (1990) The influence of bulk composition on the speciation of water in silicate glasses. *Contrib. to Mineral. Petrol.* **104**, 142–162.

Sisson T. W. and Grove T. L. (1993) Experimental investigations of the role of H_2O in calc-alkaline differentiation and subduction zone magmatism. *Contrib. to Mineral. Petrol.* **113**, 143–166.

Spilliaert N., Métrich N. and Allard P. (2006) S-Cl-F degassing pattern of water-rich alkali basalt: Modelling and relationship with eruption styles on Mount Etna volcano. *Earth Planet. Sci.*

Lett. **248**, 772–786.

Surl L., Donohoue D., Aiuppa A., Bobrowski N. and Von Glasow R. (2015) Quantification of the depletion of ozone in the plume of Mount Etna. *Atmos. Chem. Phys.* **15**, 2613–2628.

Szramek L., Gardner J. E. and Larsen J. (2006) Degassing and microlite crystallization of basaltic andesite magma erupting at Arenal Volcano, Costa Rica. *J. Volcanol. Geotherm. Res.* **157**, 182–201.

Thordarson T. and Larsen G. (2007) Volcanism in Iceland in historical time: Volcano types, eruption styles and eruptive history. *J. Geodyn.* **43**, 118–152.

Watson E. B. (2017) Diffusive fractionation of volatiles and their isotopes during bubble growth in magmas. *Contrib. to Mineral. Petrol.* **172**.

Watson E. B. and Bender J. F. (1980) Diffusion of cesium, samarium, strontium, and chlorine in molten silicate at high temperatures and pressures. *Geol. Soc. Am. Abstr. with Programs* **12**, 545.

Weber G. and Castro J. M. (2017) Phase petrology reveals shallow magma storage prior to large explosive silicic eruptions at Hekla volcano, Iceland. *Earth Planet. Sci. Lett.* **466**, 168–180.

Webster J. D., Baker D. R. and Aiuppa A. (2018) Halogens in Mafic and Intermediate-Silica Content Magmas. In *The Role of Halogens in Terrestrial and Extraterrestrial Geochemical Processes* (eds. D. E. Harlov and L. Y. Aranovich). Springer-Verlag. pp. 307–430.

Wiedenbeck M. (2017) Comment on: The F, Cl, Br and I Contents of Reference Glasses BHVO-2G, BIR-1G, BCR-2G, GSD-1G, GSE-1G, NIST SRM 610 and NIST SRM 612 by Marks et al. This Issue. *Geostand. Geoanalytical Res.* **41**, 147–152.

Yoshimura S. (2018) Chlorine diffusion in rhyolite under low-H_2O conditions. *Chem. Geol.* **483**, 619–630.

Zeng Q. and Stebbins J. F. (2000) Fluoride sites in aluminosilicate glasses: High-resolution 19F NMR results. *Am. Mineral.* **85**, 863–867.

Zhang Y. (2010) Diffusion in Minerals and Melts: Theoretical Background. *Rev. Mineral. Geochemistry* **72**, 5–59.

908 Zhang Y. and Ni H. (2010) Diffusion of H, C, and O components in silicate melts. *Rev. Mineral.*
909 *Geochemistry* **72**, 171–225.
910 Zhang Y., Ni H. and Chen Y. (2010) Diffusion data in silicate melts. *Rev. Mineral. Geochemistry* **72**,
911 311–408.
912 Zimova M. and Webb S. L. (2007) The combined effects of chlorine and fluorine on the viscosity
913 of aluminosilicate melts. *Geochim. Cosmochim. Acta* **71**, 1553–1562.
914
915

Tables

Table 1: *Major element composition of the synthesized starting glasses as determined by EPMA and SIMS analysis. All values represent units of wt.% unless otherwise stated. All data are corrected for Na-loss during EPMA analysis.*

	HX[a]		**CCX**	
	enriched (n = 15)	depleted (n = 14)	enriched (n = 6)	depleted (n = 5)
SiO_2	68.5 (4)	68.3 (3)	67.8 (3)	67.9 (5)
TiO_2	0.46 (2)	0.46 (2)	0.66 (3)	0.67 (2)
Al_2O_3	14.7 (1)	14.57 (8)	14.49 (4)	14.48 (7)
FeO	4.6 (3)	4.76 (6)	3.84 (5)	3.94 (8)
MgO	0.46 (2)	0.44 (2)	0.60 (3)	0.62 (2)
MnO	0.13 (2)	0.15 (2)	0.12 (4)	0.11 (2)
CaO	2.85 (7)	2.82 (5)	2.11 (3)	2.12 (3)
Na_2O	6.2 (2)	6.35 (7)	6.9 (1)	7.8 (1)
K_2O	2.10 (3)	2.20 (3)	2.39 (3)	2.65 (4)
F	0.53 (2)	0.04 (3)	0.96 (2)	0.03 (1)
Cl	0.26 (1)	0.02 (2)	0.4 (1)	0.04 (1)
Br	nd	nd	~ 2500 ppm	~ 1 ppm
I	nd	nd	~ 290 ppm	0
Total	100.52	100.05	99.82	100.35
NBO/T[c]	0.08	0.08	0.09	0.11

[a] Data from Feisel et al. (2019)

[b] Absolute values of Br and I estimated based on SIMS analyses and only available for CCX melts.

[c] NBO/T is calculated after (Mysen, 1988) and Giordano et al. (2008).

Table 2: *Conditions and results of all experiments. Experiments of the anhydrous series (HX and CCX) were carried out at P = 1 bar. Hydrous experiments were done at P = 160 MPa. All diffusivities in m^2 s^{-1}.*

sample	*T* [° C]	*t* [s]	H_2O [wt.%]	#	D_F	s.d.	D_{Cl}	s.d.	D_{Br}	s.d.	D_I	s.d.
HX9	750	3023535	-	1[a]	1.6×10^{-15}	4.3×10^{-16}	1.7×10^{-17}	8.4×10^{-18}				
				2[b]	1.6×10^{-15}*	3.2×10^{-16}	3.9×10^{-17}	1.1×10^{-17}	3.4×10^{-18}	8.8×10^{-19}	1.8×10^{-18}	7.8×10^{-19}
HX7	800	587235	-	1[a]	6.6×10^{-15}	1.6×10^{-16}	4.9×10^{-17}	1.4×10^{-17}				
				2[a]	1.1×10^{-14}	1.9×10^{-15}	1.6×10^{-16}	4.2×10^{-17}				
				3[b]	1.1×10^{-14}	6.0×10^{-16}	4.0×10^{-16}	6.2×10^{-17}	2.3×10^{-17}	4.7×10^{-18}		
HX3	850	171502	-	1[a]	1.6×10^{-14}	5.0×10^{-15}	3.9×10^{-16}	2.0×10^{-16}				
				2[a]	1.9×10^{-14}	5.9×10^{-15}	4.5×10^{-16}	2.4×10^{-16}				
				3[b]	2.3×10^{-14}*	4.6×10^{-15}	4.3×10^{-16}	9.7×10^{-17}	6.2×10^{-17}	2.9×10^{-17}	4.0×10^{-17}	2.1×10^{-17}
HX10	850	266855	-	1[a]	1.9×10^{-14}	4.4×10^{-15}	3.9×10^{-16}	1.2×10^{-16}				
				2[a]	2.0×10^{-14}	5.1×10^{-15}	7.4×10^{-16}	4.0×10^{-16}				
				3[b]	2.1×10^{-14}*	1.8×10^{-15}	6.2×10^{-16}	7.4×10^{-17}	8.9×10^{-17}	1.6×10^{-17}	2.7×10^{-17}	3.6×10^{-16}
HX5	900	154560	-	1[a]	4.7×10^{-14}	6.7×10^{-15}	1.0×10^{-15}	2.0×10^{-16}				
				2[a]	4.6×10^{-14}	8.9×10^{-15}	8.7×10^{-16}	1.9×10^{-16}				
				3[b]	3.2×10^{-14}*	6.2×10^{-15}	1.0×10^{-15}	1.3×10^{-16}	1.6×10^{-16}	6.5×10^{-17}		
HX8	950	87025	-	1[a]	1.3×10^{-13}	2.5×10^{-14}	4.5×10^{-15}	1.1×10^{-15}				
				2[a]	1.1×10^{-13}	1.4×10^{-14}	1.5×10^{-15}	6.7×10^{-16}				
				3[b]	1.4×10^{-13}	1.6×10^{-14}	5.9×10^{-15}	8.7×10^{-16}	1.3×10^{-15}	2.7×10^{-16}	3.9×10^{-16}	1.9×10^{-16}

[a] Results from EPMA analyses. EPMA data of HX series from Feisel et al. (2019)

[b] Results from SIMS analyses

*Asymmetric profiles were first fitted each half at a time to confirm reliability of the fit of the complete profile (see text for further discussion)

927 ***Table 2:*** *(continued)*

928

sample	*T* [° C]	*t* [s]	H_2O [wt.%]	#	D_F	s.d.	D_{Cl}	s.d.	D_{Br}	s.d.	D_I	s.d.
CCX3	850	237370	-	1[a]	6.6×10^{-14}*	1.3×10^{-14}	2.4×10^{-15}	9.0×10^{-16}				
				2[b]	3.6×10^{-14}*	1.2×10^{-14}	3.5×10^{-15}	7.1×10^{-16}	4.8×10^{-16}	7.3×10^{-17}		
CCX4	900	170880	-	1[a]	6.3×10^{-14}*	1.2×10^{-14}	1.7×10^{-15}	4.9×10^{-16}				
				2[a]	6.6×10^{-14}*	1.1×10^{-14}	5.7×10^{-15}	1.2×10^{-15}				
				3[b]	5.4×10^{-14}	1.0×10^{-14}	9.7×10^{-15}	1.4×10^{-15}	1.2×10^{-15}	1.2×10^{-16}	1.7×10^{-16}	5.9×10^{-17}
CCX1	950	82770	-	1[a]	1.1×10^{-13}*	1.6×10^{-14}	8.8×10^{-15}	1.3×10^{-15}				
				2[a]	1.2×10^{-13}*	1.9×10^{-14}	7.1×10^{-15}	1.2×10^{-15}				
				3[b]	1.1×10^{-13}*	1.4×10^{-14}	7.7×10^{-15}	7.5×10^{-16}	1.1×10^{-15}	1.3×10^{-16}	2.5×10^{-16}	1.1×10^{-16}
CCX5	1000	74069	-	1[a]	6.9×10^{-13}	6.1×10^{-14}	4.0×10^{-14}	5.9×10^{-15}				
				2[a]	5.0×10^{-13}	4.2×10^{-14}	5.8×10^{-14}	8.2×10^{-15}				
				3[a]	6.4×10^{-13}	1.4×10^{-13}	6.7×10^{-14}	2.3×10^{-14}				
				4[b]	6.7×10^{-13}	7.4×10^{-14}	7.0×10^{-14}	2.6×10^{-14}	1.3×10^{-14}	7.5×10^{-15}		
				5[b]	7.5×10^{-13}	4.4×10^{-14}	7.3×10^{-14}	4.3×10^{-15}	1.2×10^{-14}	1.3×10^{-15}	9.4×10^{-16}	1.3×10^{-16}
CCX-H-38	1000	16380	1.9 (1)	1[a]	3.3×10^{-12}	4.2×10^{-13}	4.3×10^{-13}	1.4×10^{-13}				
				2[b]	3.3×10^{-12}	1.6×10^{-13}	5.4×10^{-13}	3.7×10^{-14}	2.5×10^{-13}	1.6×10^{-14}	9.4×10^{-14}	8.1×10^{-15}
CCX-H-40	1050	10200	1.9 (1)	1[a]	6.2×10^{-12}	9.6×10^{-13}	9.2×10^{-13}	2.2×10^{-13}				
				2[b]	6.6×10^{-12}	2.6×10^{-13}	1.3×10^{-12}	1.4×10^{-13}	5.8×10^{-13}	6.8×10^{-14}	2.3×10^{-13}	2.9×10^{-14}
CCX-H-42	1100	8100	1.5 (1)	1[a]	5.5×10^{-12}	7.7×10^{-13}	7.9×10^{-13}	1.6×10^{-13}				
				2[b]	5.3×10^{-12}	1.3×10^{-13}	9.5×10^{-13}	2.3×10^{-13}	4.2×10^{-13}	3.8×10^{-14}	1.6×10^{-13}	2.4×10^{-14}
CCX-H-43	1150	6000	2.1 (2)	1[a]	1.3×10^{-11}	1.4×10^{-12}	4.2×10^{-12}	6.7×10^{-13}				
				2[b]	1.3×10^{-11}	4.4×10^{-13}	3.6×10^{-12}	2.4×10^{-13}	1.6×10^{-12}	9.3×10^{-14}	6.5×10^{-13}	6.7×10^{-14}
CCX-H-44	1200	4800	2.0 (2)	1[a]	1.9×10^{-11}	2.0×10^{-12}	7.6×10^{-12}	1.3×10^{-12}				
				2[b]	2.0×10^{-11}	1.1×10^{-12}	7.7×10^{-12}	8.5×10^{-13}	3.9×10^{-12}	4.8×10^{-13}	2.1×10^{-12}	4.2×10^{-13}

***Table 3**: Arrhenius parameters of all halogens and oxygen self-diffusion in all investigated melt compositions. D_0 is given in $m^2\ s^{-1}$ and E_A is given in $kJ\ mol^{-1}$. Calculation of Eyring diffusivities is described in the text.*

	HX			CCX			CCX-H		
	D_0	**E_A**	**+/-**	**D_0**	**E_A**	**+/-**	**D_0**	**E_A**	**+/-**
F	1.50e-4	212.7	28	5.11e-5	197.5	99.4	7.76e-7	131.0	38.0
Cl	1.24e-4	245.8	51	5.10e-5	222.6	112	1.74e-4	210.1	67.6
Br	1.78e-3	287.6	66.5	1.16e-5	225.2	367.8	3.97e-5	201.4	153.5
I	3.50e-4	280.0	63.8	2.51e-7	207.4	973.2	1.02e-4	222.2	180.2
O_{Eyring}	6.9e-1	399.1	26.4	1.43e-1	375.5	22.0	-	-	-

Figures

935

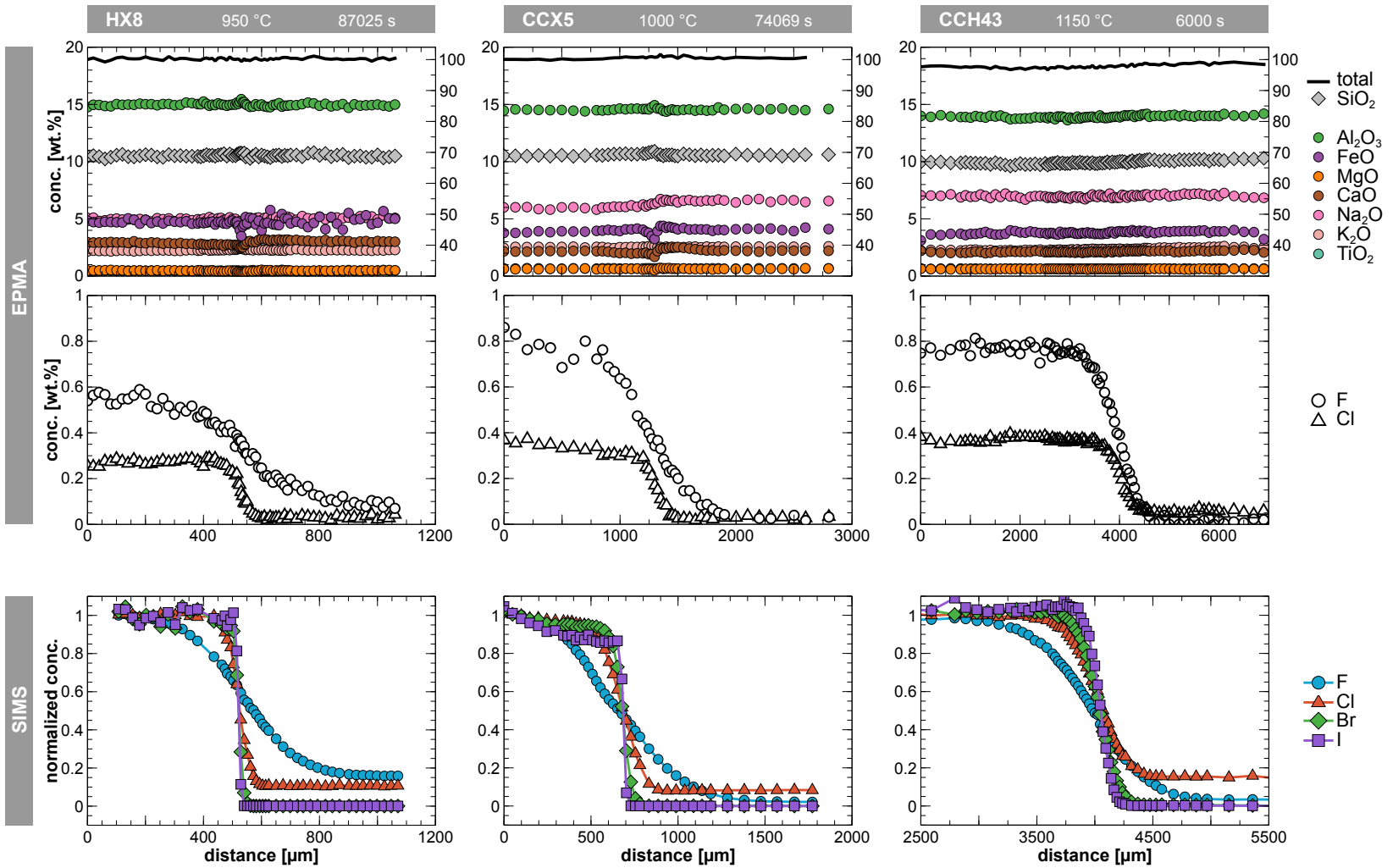

Fig. 1: *Concentration vs. distance diagrams of one sample of each investigated melt composition acquired by EPMA and SIMS analyses. In the upper row, data of SiO_2 and totals refer to the secondary y-axis. EPMA data represents absolute values whereas the SIMS data was normalized to the average of the 4 outermost datapoints of each respective halogen in the enriched diffusion couple half. This way it is possible to visualize all halogens of a sample in one diagram.*

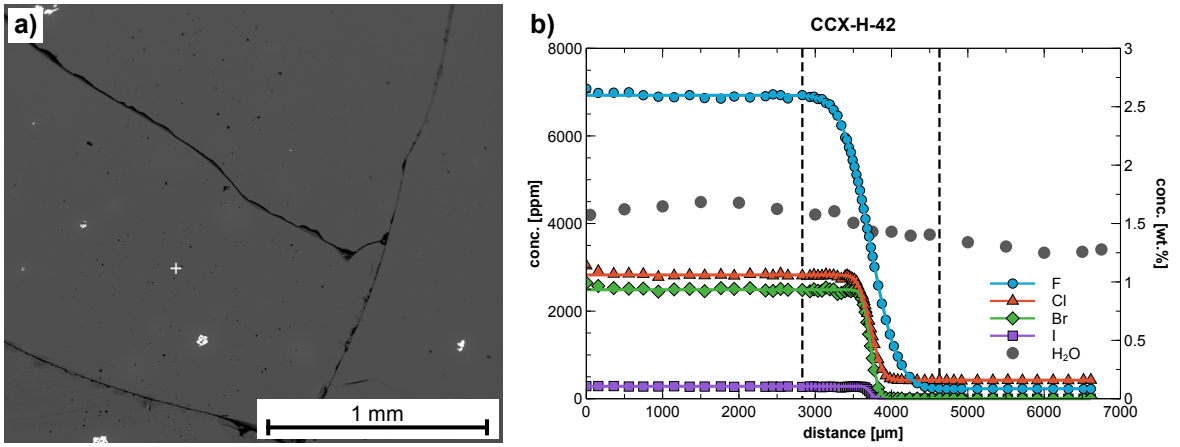

Fig. 2: *Backscattered image and diffusion profiles of sample CCX-H-42.* ***a)*** *Backscattered image of the center part of sample CCX-H-42 showing minor cracks likely caused during rapid quench (few seconds).* ***b)*** *Concentration vs. distance profiles of F, Cl, Br, I and H_2O as acquired by SIMS. The halogen data are plotted together with their respective fit curves calculated using equation 1. Diagrams of the other CCX-H samples are provided in the supplementary material.*

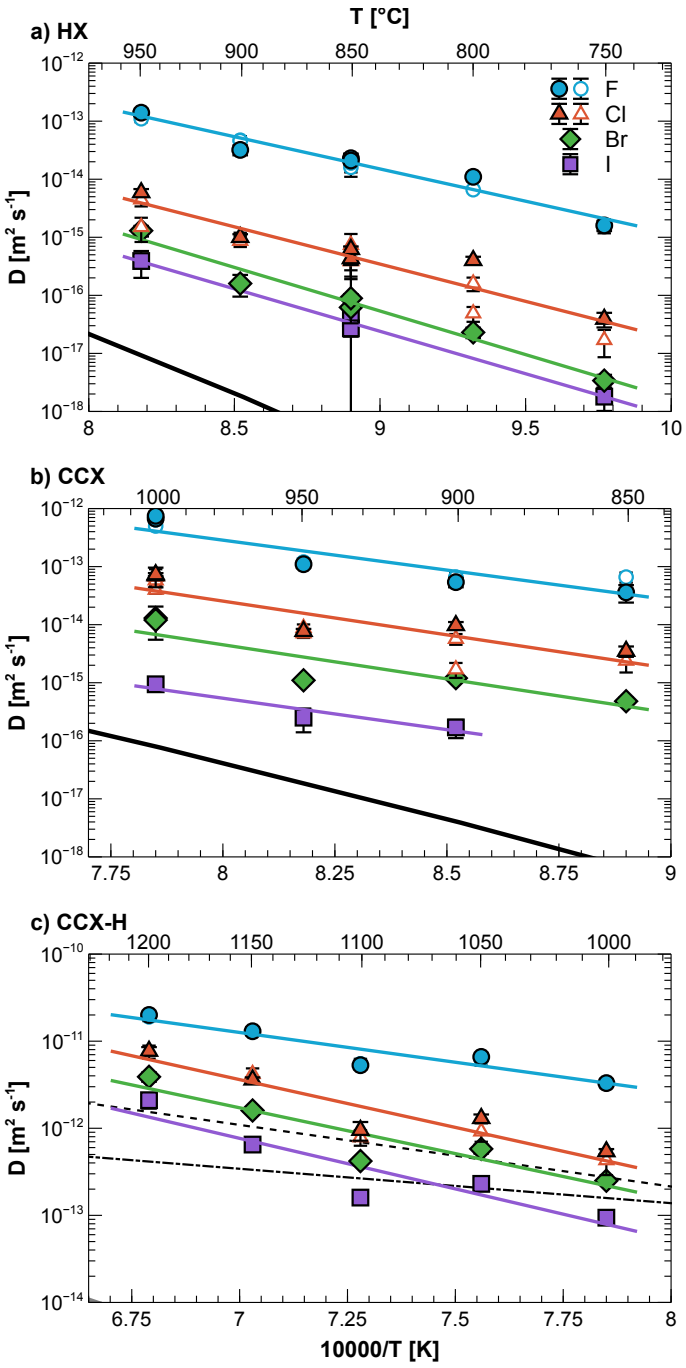

Fig. 3: *Arrhenius diagrams of all investigated melt compositions illustrating the individual diffusion coefficients and the corresponding Arrhenius fits of all halogens.* ***a)*** *anhydrous HX melt.* ***b)*** *anhydrous CCX melt.* ***c)*** *hydrous CCX melt (~1.5 wt.% H_2O). The bold black lines indicate the self-diffusivity of oxygen calculated with the Eyring-equation and based on the calculated viscosities of the anhydrous melt compositions* (Giordano et al., 2008)*. The dashed lines in c) indicate calculated oxygen self-diffusion in Rhyolite (dash-dot) and Dacite (dashed) from* (Zhang and Ni, 2010)*. Open symbols represent data based on EPMA analyses.*

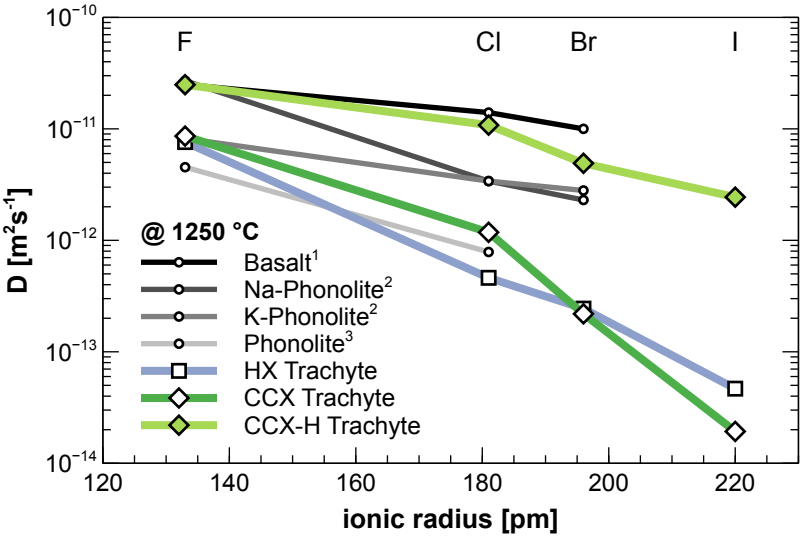

953

954 ***Fig. 4:*** *Halogen diffusivity at 1250 °C of the melts of this and other published studies plotted*
955 *relative to the ionic radius of the respective halogen. All data are for anhydrous compositions*
956 *except the hydrous data of the present study. Diffusivities at 1250 °C were calculated from the*
957 *respective Arrhenius parameters of each composition and halogen. Data from:* [1] Alletti et al.,
958 (2007)*;* [2] Balcone-Boissard et al., (2009) and Balcone-Boissard et al., (2020)*;* [3] Böhm and
959 Schmidt, (2013)

960

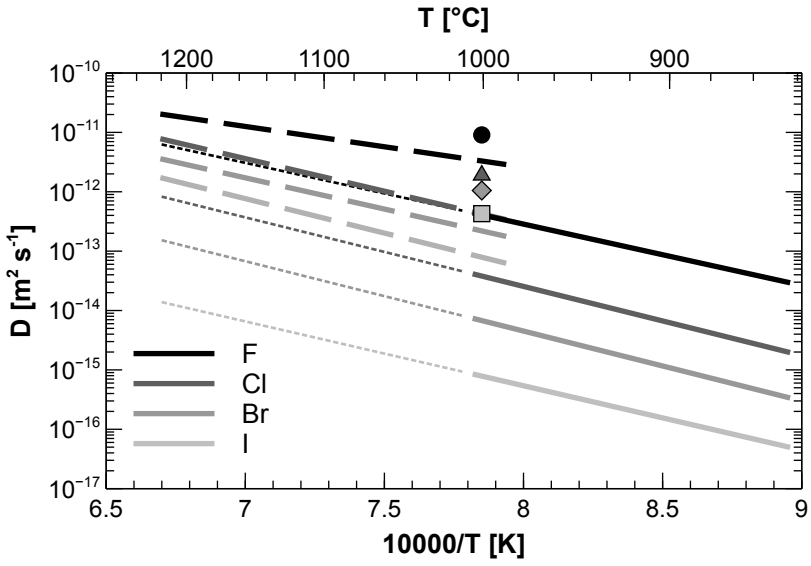

961 .

962 ***Fig. 5:*** *Comparative Arrhenius diagram of halogen diffusion in anhydrous and hydrous (1.5 wt.%*
963 *H_2O) trachytic melt determined in this study. Solid lines represent diffusion in anhydrous melt and*
964 *dotted lines indicate extrapolation to higher temperatures. Long-dashed lines represent diffusion*
965 *in hydrous melt. Solid symbols show preliminary results of halogen diffusion in melt containing 3.5*
966 *wt.% H_2O. Note that the diffusivity of all halogens is even more enhanced in the more strongly*
967 *hydrated melt.*

968